




Article

In Silico Investigation of the Impact of Hole-Transport Layers on the Performance of $\text{CH}_3\text{NH}_3\text{SnI}_3$ Perovskite Photovoltaic Cells

Zhansaya Omarova ¹, Darkhan Yerezhep ^{1,*} , Abdurakhman Aldiyarov ¹  and Nurlan Tokmoldin ² 

¹ Faculty of Physics and Technology, Al Farabi Kazakh National University, 71 Al-Farabi Ave., Almaty 050040, Kazakhstan; zhansaya_o@mail.ru (Z.O.); abdurakhman.aldiyarov@kaznu.kz (A.A.)

² Optoelectronics of Disordered Semiconductors, Institute of Physics and Astronomy, University of Potsdam, Karl-Liebknecht-Straße 24–25, 14476 Potsdam-Golm, Germany; tokmoldin@uni-potsdam.de

* Correspondence: darhan_13@physics.kz

Abstract: Perovskite solar cells represent one of the recent success stories in photovoltaics. The device efficiency has been steadily increasing over the past years, but further work is needed to enhance the performance, for example, through the reduction of defects to prevent carrier recombination. SCAPS-1D simulations were performed to assess efficiency limits and identify approaches to decrease the impact of defects, through the selection of an optimal hole-transport material and a hole-collecting electrode. Particular attention was given to evaluation of the influence of bulk defects within light-absorbing $\text{CH}_3\text{NH}_3\text{SnI}_3$ layers. In addition, the study demonstrates the influence of interface defects at the $\text{TiO}_2/\text{CH}_3\text{NH}_3\text{SnI}_3$ (IL1) and $\text{CH}_3\text{NH}_3\text{SnI}_3/\text{HTL}$ (IL2) interfaces across the similar range of defect densities. Finally, the optimal device architecture $\text{TiO}_2/\text{CH}_3\text{NH}_3\text{SnI}_3/\text{Cu}_2\text{O}$ is proposed for the given absorber layer using the readily available Cu_2O hole-transporting material with $PCE = 27.95\%$, $FF = 84.05\%$, $V_{OC} = 1.02$ V and $J_{SC} = 32.60$ mA/cm², providing optimal performance and enhanced resistance to defects.

Keywords: perovskite solar cells; $\text{CH}_3\text{NH}_3\text{SnI}_3$; SCAPS-1D; modeling; HTL



Citation: Omarova, Z.; Yerezhep, D.; Aldiyarov, A.; Tokmoldin, N. In Silico Investigation of the Impact of Hole-Transport Layers on the Performance of $\text{CH}_3\text{NH}_3\text{SnI}_3$ Perovskite Photovoltaic Cells. *Crystals* **2022**, *12*, 699. <https://doi.org/10.3390/cryst12050699>

Academic Editors: Vishal Gupta and Surendra Kumar Yadav

Received: 22 April 2022

Accepted: 12 May 2022

Published: 14 May 2022

Publisher's Note: MDPI stays neutral with regard to jurisdictional claims in published maps and institutional affiliations.



Copyright: © 2022 by the authors. Licensee MDPI, Basel, Switzerland. This article is an open access article distributed under the terms and conditions of the Creative Commons Attribution (CC BY) license (<https://creativecommons.org/licenses/by/4.0/>).

1. Introduction

Photovoltaic cells based on crystalline silicon have proven themselves at the industrial scale as a viable alternative energy source due to their high performance, material abundance and proven microelectronic technology [1–3]. At the same time, in spite of the excellent power conversion efficiencies [4–6], the technology still requires further improvement through reduction in costs, facilitation of the manufacturing steps and minimization of the environmental pollution associated with the production process [7–9]. In recent years, perovskite solar cells (PSC) based on organometallic lead halides have emerged as strong competitors to silicon in the photovoltaic market [10–12], as well as an efficient technology to complement the silicon photovoltaic devices in tandem architecture [13–15]. These materials boast high efficiency (about 25%) at a fraction of the silicon device thickness, as well as ease of fabrication, making them highly promising for future photovoltaic applications [16–22]. One of the main downsides of these devices is that the best efficiencies have so far been demonstrated by organometallic lead halides which present a serious danger to the environment due to the toxicity of lead [23–25]. Thus, replacing elemental lead with environmentally friendly alternatives in the perovskite lattice is a pressing problem in photovoltaics [26,27].

A significant amount of research is being dedicated to developing lead-free PSC, with the tin halide perovskite being one of the most promising alternatives [28–31]. Tin is widely distributed in nature and has similar electronic properties to lead, since it is a member of the same group in the periodic table [32,33]. In addition, perovskites based on tin halide

have excellent light absorbing properties and high carrier mobilities [34–36]. Additionally, tin-based perovskites provide a high theoretical PCE due to a smaller band gap than the equivalent lead-based perovskites [37].

A PSC in most cases consists of an absorbing layer and two transport layers—an electron transport layer (ETL) and a hole transport layer (HTL), which perform the function of collecting charge carriers [38]. The device structure is completed with a transparent conducting electrode on top of a glass substrate, on the one side, and a metal electrode (such as Au, Ag, Al, etc.), on the other. To be efficient, the transport layers must possess certain properties: above all, high transparency and a high selective charge transport. As such, determination of the optimal properties of an ETL and an HTL plays an important role in maximizing the PSC performance and maintaining the device stability [39].

So far, a variety of transport layers have been tested, ranging from metal-oxides and fullerenes to organic materials and self-assembled monolayers [19,40–43]. For example, TiO_2 has been a popular choice for an ETL in the n-i-p device configuration, due to its chemical stability, good electron transport, efficient hole-blocking at the interface and environmental friendliness [44–46]. On the other side, a significant effort has also been placed on the development and optimization of HTLs. Efficient HTL materials should possess the following properties [47–50]:

1. high carrier mobility to increase the fill factor (FF);
2. a wide optical band gap and high transparency to minimize optical losses;
3. high resistance to water, light and heat;
4. low cost of materials and production;
5. environmental friendliness.

The hole transport layers must be chosen thoughtfully to prevent charge recombination at the interfacial layer boundaries and ensure high device performance. At the same time, it is very important that their fabrication is compatible with the low-cost deposition, solution-processability and flexibility, similar to the other layers within the perovskite cell structure. We thus selected three HTL layers, which are commonly used in perovskite-based solar cells: Spiro-OMeTAD [51–54], PEDOT:PSS [55–57] and Cu_2O [58–60]. It must be noted that whilst the former two materials can be deposited in a straightforward fashion from, respectively, organic or aqueous solvents, the current approach to solution deposition of Cu_2O is more complicated, initially involving the deposition of CuI following its further chemical conversion to Cu_2O [61]. We nevertheless consider this metal-oxide HTL in our study due to its high performance and versatility.

Further improvement in the device power conversion efficiency (PCE) requires a detailed understanding of the PSC working mechanism, based not only on experimental research, which may end up being expensive and time-consuming, but also on device simulation [62–70]. A limited number of studies focusing on the simulation of lead-free PSCs, as well as on the optimization of their charge-transport layers, has been conducted so far [71–75]. In this article, a cell architecture has been selected using $\text{CH}_3\text{NH}_3\text{SnI}_3$ as an absorbing layer with three different HTLs, namely 2,2',7,7'-Tetrakis-(*N,N*-di-*p*-methoxyphenylamine) 9,9'-spirobifluorene (Spiro-OMETAD), poly(3,4-ethylenedioxythiophene)-poly(styrene sulfonate) (PEDOT:PSS) and cuprous oxide (Cu_2O). Moreover, we consider the applicability of various metal back contacts, such as Al, Ti, Cr, Ag, Ni, Cu, C, Au and Pt. In the presented numerical study, various PSC configurations are defined and evaluated using the SCAPS 1D simulator.

2. Method

The crystal structure of the tin-based perovskite $\text{CH}_3\text{NH}_3\text{SnI}_3$ employed in this study as the absorber layer is shown in Figure 1. The simulated photovoltaic cell configurations are as follows (Figure 2):

- Structure 1. $\text{TiO}_2/\text{CH}_3\text{NH}_3\text{SnI}_3/\text{Spiro-OMETAD}$;
- Structure 2. $\text{TiO}_2/\text{CH}_3\text{NH}_3\text{SnI}_3/\text{PEDOT:PSS}$;
- Structure 3. $\text{TiO}_2/\text{CH}_3\text{NH}_3\text{SnI}_3/\text{Cu}_2\text{O}$.

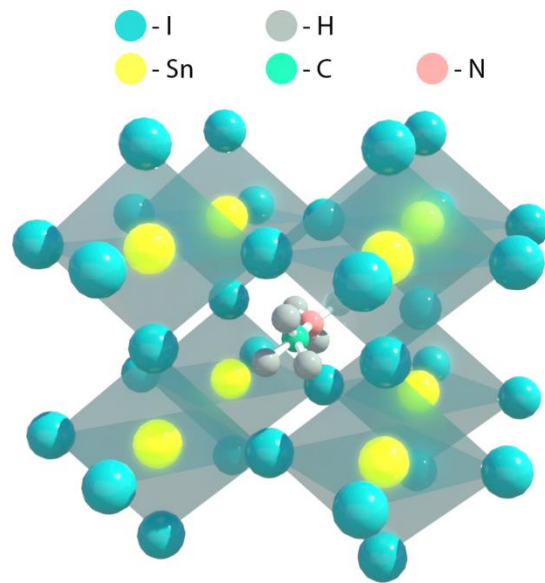


Figure 1. Unit cell of tin-based perovskite.

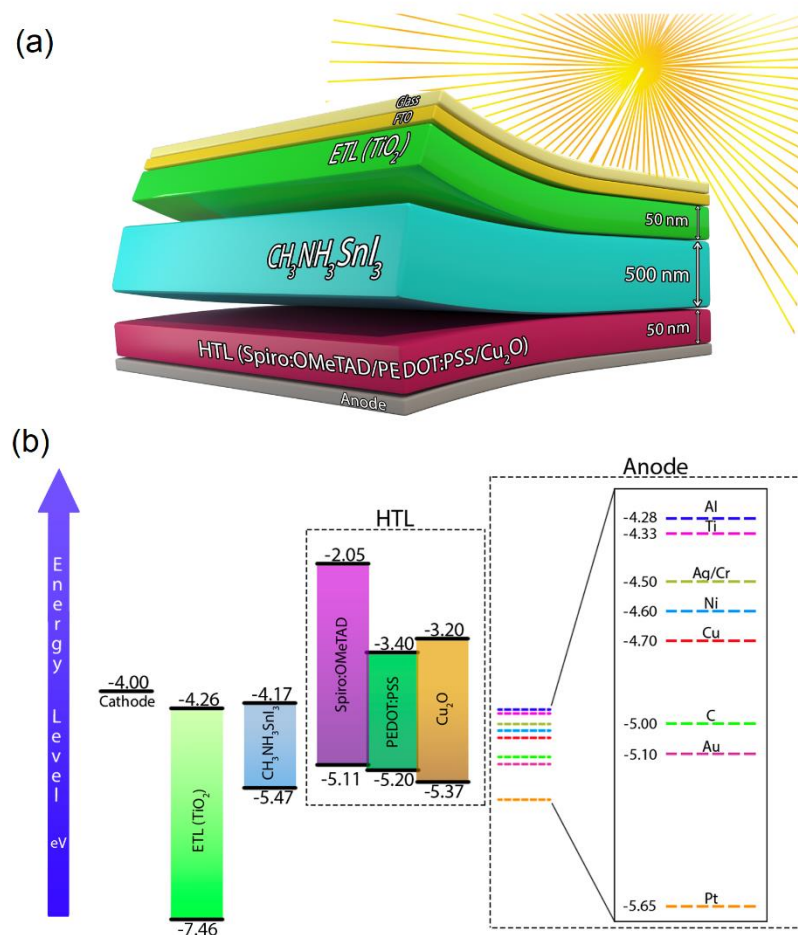


Figure 2. Schematic diagram of the studied perovskite solar cell (a) and energy band alignment (b).

For all simulations of the photovoltaic cell under illumination the standard photovoltaic radiation spectrum AM 1.5G was used (1000 W/m^2 , $T = 300 \text{ K}$). The $\text{CH}_3\text{NH}_3\text{SnI}_3$ layer thickness remained fixed and equal to 500 nm.

Numerical simulation has proved to be an important tool for understanding the physical properties and design of a variety of solar cells based on crystalline, polycrystalline

and amorphous materials [76–78]. Among numerical analysis instruments, SCAPS-1D (ELIS, University of Ghent, Belgium) has recently become popular, as it has proven its effectiveness in simulating a variety of research systems [25,42,62–65,76,79]. The SCAPS-1D software uses a combination of mathematical equations, including the Poisson equation, continuity equations, total charge transfer equations, whose detailed description can be found elsewhere [80,81].

The parameters of the simulated photovoltaic cell are presented in Table 1 and are based on the published literature [53,82–85].

Table 1. Parameters of solar cells.

Parameters	FTO	TiO ₂	CH ₃ NH ₃ SnI ₃	Spiro-OMeTAD	PEDOT:PSS	Cu ₂ O
Thickness (nm)	500	50 *	300–1300 *	50 *	50 *	50 *
Band gap (eV)	3.50	3.20	1.30	3.06	1.80	2.17
Electron affinity (eV)	4.00	4.26	4.17	2.05	3.40	3.20
Relative dielectric permittivity	9.00	9.00	8.20	3.00	18.00	7.10
Conduction band effective density of states (cm ⁻³)	2.20×10^{18}	2.20×10^{18}	1×10^{18}	2.20×10^{18}	2.20×10^{18}	2.00×10^{17}
Valence band effective density of states (cm ⁻³)	1.80×10^{19}	1.80×10^{19}	1×10^{18}	1.80×10^{19}	1.80×10^{19}	1.10×10^{19}
Electron thermal velocity (cm/s)	10^7	10^7	10^7	10^7	10^7	10^7
Hole thermal velocity (cm/s)	10^7	10^7	10^7	10^7	10^7	10^7
Electron mobility (cm ² /Vs)	20.00	20.00	1.60	2.00×10^{-4}	4.50×10^{-2}	200.00
Hole mobility (cm ² /Vs)	10.00	10.00	1.60	2.00×10^{-4}	4.50×10^{-2}	80.00
Shallow donor density N _D (cm ⁻³)	2.00×10^{19}	10^{18}	0	0	0	0
Shallow acceptor density N _A (cm ⁻³)	0	0	1.00×10^{14}	1.00×10^{18}	1.00×10^{20}	1.00×10^{18}
References	[53,82]	[83]	[82,83]	[53]	[84,85]	[53,83]

* In this study.

3. Results

3.1. Influence of Bulk Defect Density on J_{SC} , V_{OC} , FF, PCE in the Absorber Layer

We start with the study of sensitivity of the performance of PSCs having different HTLs towards the presence of bulk defects within the perovskite layer. In the manufacture of perovskite films, various defects may arise, which have a detrimental impact upon the device performance [86]. Depending on their location, defects are characterized as being deep or shallow. Shallow defects do not usually have a significant impact, whereas deep defects have a more detrimental influence on the device performance, as they are located close to the center of the band gap and trap both types of carriers (holes and electrons), thereby allowing sufficient time for recombination [87,88]. Thus, approximately 10^{10} – 10^{13} cm⁻³ can be identified as shallow defects, and deep defects starting from the defect density of 10^{14} cm⁻³ and up to about 10^{16} cm⁻³ [89,90]. Deep defects are located at the center of the band gap, i.e., at approximately 0.65 eV to 0.76 eV above the edge of the valence band, depending on the material [91]. To study the impact of bulk defects on the perovskite efficiency, the energy level position was chosen to be located at 0.6 eV above the valence band with the concentration range between 10^{10} cm⁻³ and 10^{17} cm⁻³.

Bulk defects are introduced to explain the influence of internal defects on the properties of semiconductors, including fixing the Fermi energy on the surface of semiconductor materials, stabilization of the Fermi energy, and formation of Schottky barriers [92]. Fig-

ure 3 shows the impact of the bulk defect density on the parameters of the $\text{CH}_3\text{NH}_3\text{SnI}_3$ based solar cells with different HTLs in the defect concentration range from 10^{10} cm^{-3} to 10^{17} cm^{-3} . As seen in Figure 3a–c, the device parameters (J_{SC} , V_{OC} and FF) remain unchanged at defect concentrations below 10^{13} cm^{-3} , followed by a sharp decrease at higher defect concentrations. The increase to 10^{17} cm^{-3} results in a rather similar reduction in V_{OC} from 1.0 V to 0.7 V (Figure 3b) and J_{SC} from 32 mA/cm^2 to below 25 mA/cm^2 for all of the three device structures (Figure 3a). The largest difference is observed for FF , with Structure 1 showing the lower initial value of 86%, compared to 88% for the other structures, and a stronger decrease to 37%, compared to 46% for Structure 3. As a result, the increase in bulk defect concentration from 10^{10} cm^{-3} to 10^{17} cm^{-3} leads to a reduction in PCE from around 29% to 6%, 7% and 8%, respectively, for Structures 1, 2 and 3 (Figure 3d). The bulk defects act as recombination centers for charge carriers, which is responsible for the loss in the open-circuit voltage. At the same time, the respective charge trapping on these centers may also lead to a reduction in effective carrier mobility, causing a drop in J_{SC} and FF .

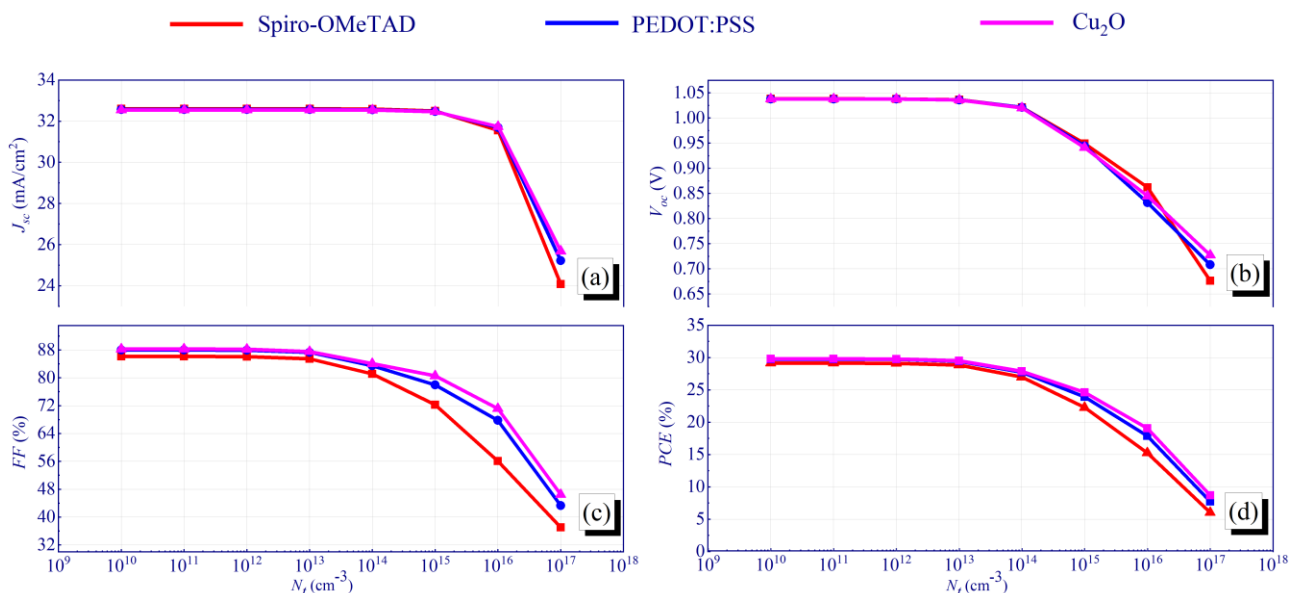


Figure 3. Influence of the bulk defect concentration (N_t) on the performance parameters of the $\text{CH}_3\text{NH}_3\text{SnI}_3$ -based solar cell with various hole-transporting layers: (a) J_{SC} , (b) V_{OC} , (c) FF , (d) PCE .

3.2. Influence of the Density on J_{SC} , V_{OC} , FF , PCE of Interfacial Defects

Interfacial recombination is known to be one of the major factors affecting the performance of PSCs [93–95]. To this end, we performed a study on the influence of the density of interfacial defects at both interfaces of the perovskite layer, $\text{TiO}_2/\text{CH}_3\text{NH}_3\text{SnI}_3$ (IL1) and $\text{CH}_3\text{NH}_3\text{SnI}_3/\text{HTL}$ (IL2), on the efficiency of devices with different HTLs (Figure 4). The total density (N_i) of interfacial defects varied in the range from 10^{10} cm^{-2} to 10^{17} cm^{-2} . Within this range, V_{OC} drops insignificantly for all the device structures (Figure 4b). Surprisingly, the device performance remains unchanged in a wide range of interface defect concentrations up to 10^{15} cm^{-2} . Further increase to 10^{17} cm^{-2} results in a sharp decrease in the performance for all the device structures. It must be noted that the FF of Structure 3 remains relatively stable for the studied range of interface defect concentrations. For all the structures, there are no significant changes in FF up to N_i of 10^{16} cm^{-2} ; above this density there is a slight decrease in FF from 81% to 78%, from 83% to 82% and from 84% to 83%, for Structures 1, 2 and 3, respectively (see Figure 4c).

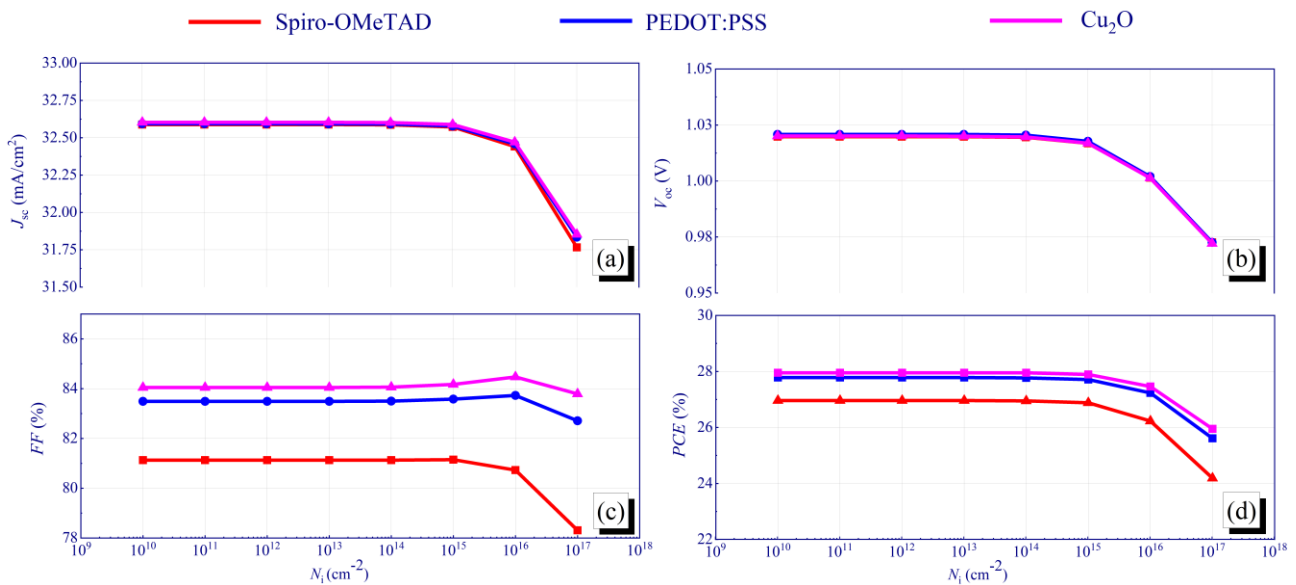


Figure 4. Influence of the concentration of interfacial defects (N_i) at the $\text{TiO}_2/\text{CH}_3\text{NH}_3\text{SnI}_3$ (IL1) and $\text{CH}_3\text{NH}_3\text{SnI}_3/\text{HTL}$ (IL2) interfaces: (a) J_{SC} , (b) V_{OC} , (c) FF , (d) PCE .

Next, we simulated the impact of N_i in the range from 10^{10} to 10^{17} cm^{-2} at the ETL/perovskite and perovskite/HTL interfaces. N_t was chosen to be 10^{14} cm^{-3} throughout the entire numerical experiment. Figure 5b,d shows a decrease in V_{OC} and PCE with increasing N_i at the ETL/perovskite interface for the devices with different HTLs. When the density of the defect states at the interface reaches 10^{17} cm^{-2} , we observe a faster decrease in the efficiency of the Spiro-OMeTAD based PSC (from 27% to 19%). For the PEDOT:PSS and Cu_2O layers, the decrease is less significant (from 28% to 22% and 28% to 24%, respectively). J_{SC} and FF , however, do not show a noticeable decrease for the selected range of defect concentrations (Figure 5a,c). It should also be noted that in the N_i range from 10^{11} cm^{-2} to 10^{16} cm^{-2} , a rise in FF is observed for all the HTLs. For example, for the Cu_2O and PEDOT:PSS layers, the highest FF value of 86% is observed for N_i in the range of 10^{14} – 10^{15} cm^{-2} . It may be concluded that the allowable concentration of interfacial defects N_i for the $\text{TiO}_2/\text{CH}_3\text{NH}_3\text{SnI}_3$ (IL1) interface is 10^{14} cm^{-2} , since the efficiency of the photovoltaic cell deteriorates greatly beyond this level. At the defect density of 10^{14} cm^{-2} , the optimal Cu_2O HTL demonstrates the following photovoltaic characteristics: $J_{SC} = 32.5$ mA/cm^2 , $V_{OC} = 0.8$ V, $FF = 83\%$, $PCE = 24\%$.

Separately, we studied the influence of the density of defect states at the HTL/perovskite interface (Figure 6). Surprisingly, the influence of the density of interfacial defects at the IL2 interface is more pronounced than at the IL1 interface. Upon a change in the HTL, the change in V_{OC} with an increase in the density of defects has a similar character, as in the case of the IL1 interface (Figure 6b). When N_i reaches 10^{17} cm^{-2} , V_{OC} drops from 1.0 V to 0.7 V for the Spiro-OMeTAD layer, from 1.0 V to 0.8 V for the PEDOT:PSS layer, and from 1.0 V up to 0.9 V for the Cu_2O layer. The density of the defect states at the HTL/perovskite interface had no significant impact on J_{SC} up to 10^{15} cm^{-2} (Figure 6a). Above this concentration, J_{SC} decreases sharply for all the studied device structures. Figure 6c shows the dependence of FF with increasing N_i . Similar to Figure 5c, an increase in N_i to 10^{15} cm^{-2} entails an increase in the FF value. For the Spiro-OMeTAD HTL the peak FF value is 84% at N_i of 10^{13} cm^{-2} , for PEDOT:PSS—86% at N_i of 10^{14} cm^{-2} , and for Cu_2O —86% at a N_i of 10^{15} cm^{-2} . PCE decreases with increasing N_i for all the structures with different HTLs, as depicted in Figure 6d. Thus, for the Spiro-OMeTAD layer, PCE decreases from 27% to 18%, for PEDOT:PSS—from 28% to 21%, and for Cu_2O —from 28% to 23% with an increase in the density of defects from 10^{10} cm^{-2} to 10^{17} cm^{-2} .

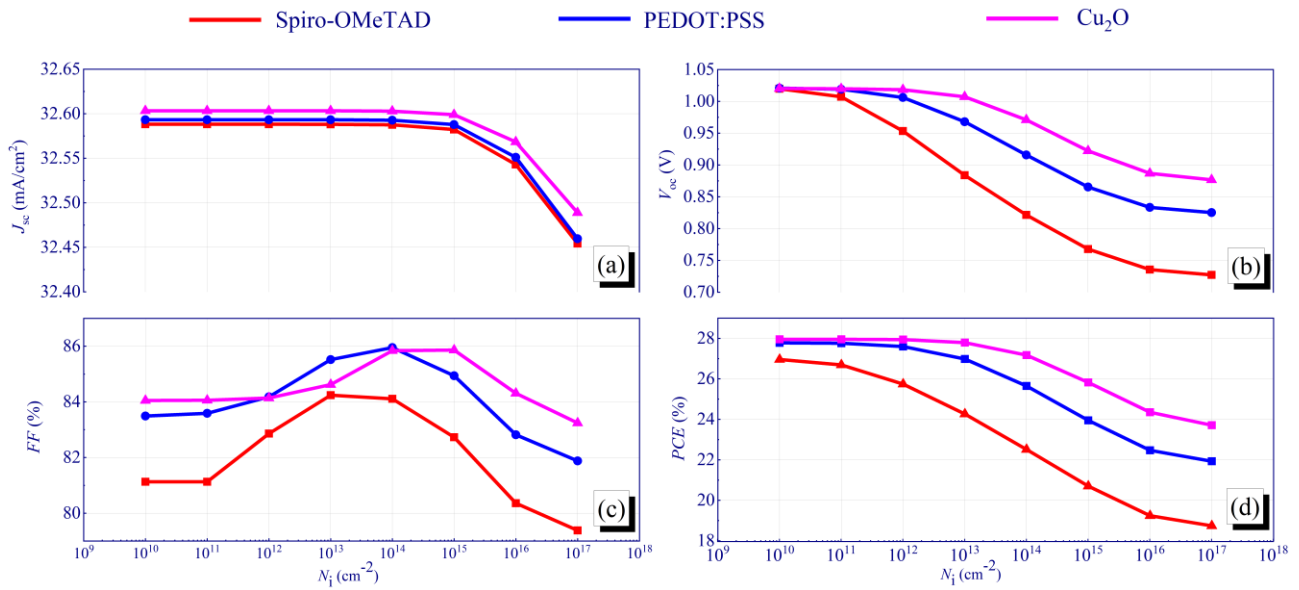


Figure 5. Influence of the concentration of interfacial defects (N_i) at the $\text{TiO}_2/\text{CH}_3\text{NH}_3\text{SnI}_3$ (IL1) interface: (a) J_{sc} , (b) V_{oc} , (c) FF, (d) PCE.

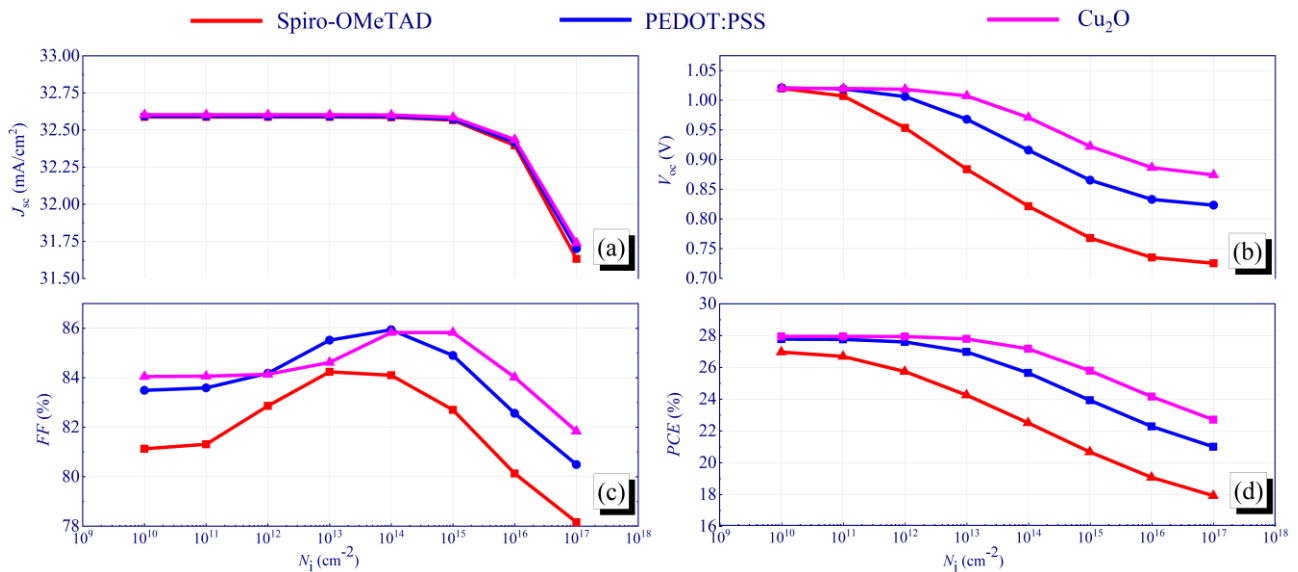


Figure 6. Influence of the concentration of interfacial defects (N_i) at the $\text{CH}_3\text{NH}_3\text{SnI}_3/\text{HTL}$ (IL2) interface: (a) J_{sc} , (b) V_{oc} , (c) FF, (d) PCE.

The allowable limit of N_i achieved prior to a rapid performance decrease for Structure 1 is 10^{13} cm^{-2} , for Structure 2— 10^{14} cm^{-2} and for Structure 3— 10^{15} cm^{-2} . The difference in the limits of resistance towards defects, depending on the HTL, is associated with various degrees of recombination of charge carriers at the interface. A high limit of resistance towards defects at the $\text{TiO}_2/\text{CH}_3\text{NH}_3\text{SnI}_3$ interface indicates good matching of the conduction band levels for the adjacent materials. It is thus concluded that an increase in the density of bulk defects within the active perovskite layer ($\text{CH}_3\text{NH}_3\text{SnI}_3$) affects the device performance more strongly than the increase in the number of interfacial defects, regardless of the choice of an HTL material. These results provide a quantitative understanding of the threshold defect density values for different perovskite cell structures. To increase the overall cell efficiency, the recombination loss at the interfaces must be reduced [96].

3.3. Influence of the Metal Contact on the Device Performance

Selection of an optimal top metal contact is an important route towards increasing the economic feasibility of a PSC. The main parameter to be varied in this respect is the metal contact work function, which characterizes the amount of energy required to extract an electron from the surface of a metal contact [97]. In this work, various metals with work functions ranging from 4.28 eV (Al) to 5.65 eV (Pt) have been studied (Table 2) [68,97–99]. The work function value is directly related to the height of the energy barrier at the metal/charge-transport layer interface affecting the ohmic nature of the contact and the resulting solar cell efficiency (Figure 7).

Table 2. Work function of a back contact metal.

Back Contact Metals	Al	Ti	Cr	Ag	Ni	Cu	C	Au	Pt
Work Function (eV)	4.28	4.33	4.50	4.50	4.60	4.70	5.00	5.10	5.65
References	[98]	[99]	[98]	[97]	[98]	[97]	[68]	[98]	[99]

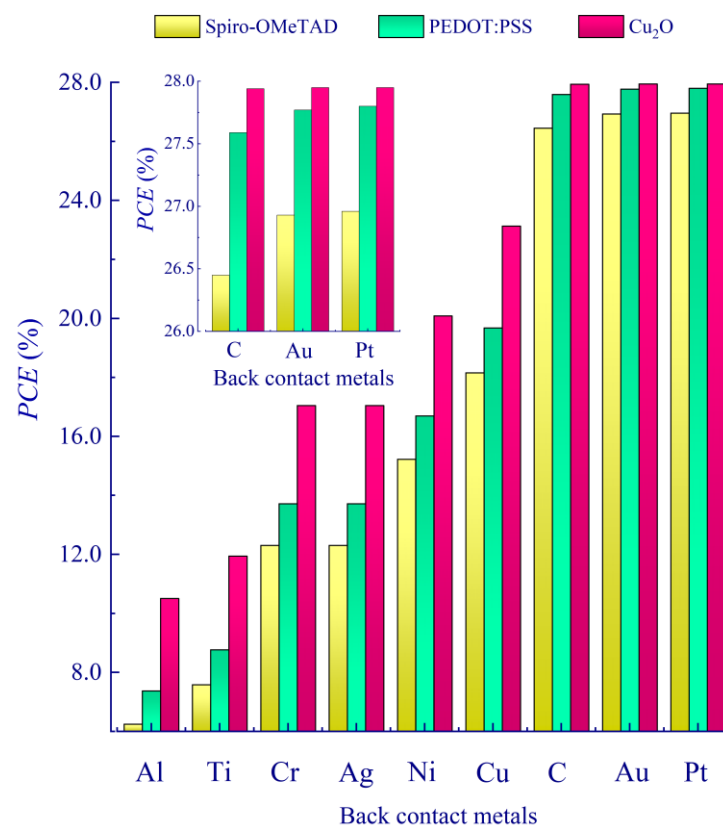


Figure 7. Perovskite solar cells efficiency depending on the choice of a back metal contact.

Based on the simulation results, the highest performance with *PCE* of ~28% is demonstrated by metals with work functions ranging from 5.00 eV to 5.65 eV. For example, using a conventional Au contact (5.10 eV), the following efficiencies are achieved for various HTLs: 26.9% (Spiro-OMeTAD), 27.8% (PEDOT:PSS) and 27.9% (Cu₂O). Figure 8 shows the *J-V* characteristic curves for the devices featuring different HTLs. The Spiro-OMeTAD layer shows the least efficient performance, suggesting that its replacement with PEDOT:PSS or Cu₂O is justified.

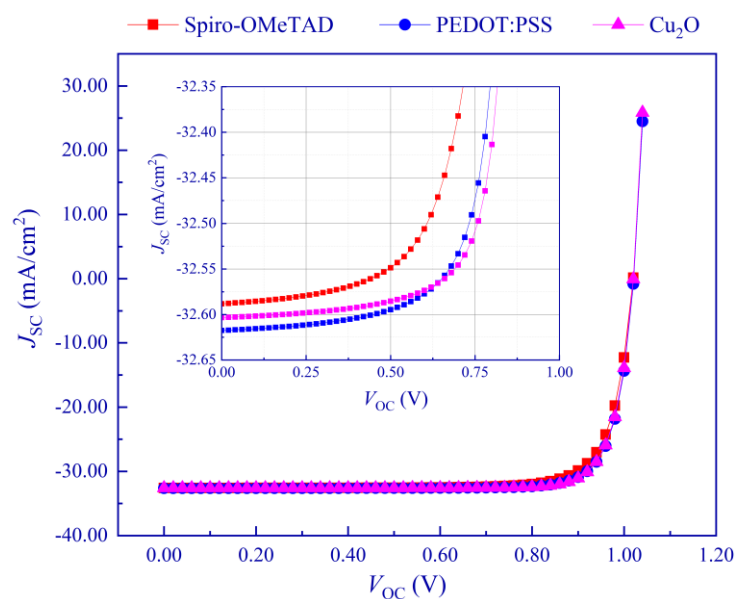


Figure 8. Current-voltage characteristics of perovskite solar cells with different hole-transport layers and a Pt back contact.

3.4. Influence of Temperature on the Device Performance

One of the main hindrances in the widespread commercialization of perovskite solar cells is their long-term stability. Most perovskites do not undergo any phase transitions, which may affect their performance, over a wide temperature range. This suggests that the main cause of thermal degradation in PSCs is not a phase transition, but the decomposition of the perovskite material. The perovskite components are known to be connected by relatively weak ionic bonds, hydrogen bonds and van der Waals forces [100]. Weak interconnections, under the influence of the atmosphere, heat and light radiation, inevitably lead to the material destruction [101]. Herein, we focus on the study of the device thermal stability in the absence of chemical degradation in the temperature range of 290–400 K. Figure 9 shows the impact of temperature on the performance of a PSC for various HTLs. A gradual decrease in all parameters with increasing temperature can be observed for all three device structures. On average, the temperature increase from 290 K to 400 K results in a perovskite *PCE* decrease of 5% in the absolute value. Cu_2O shows the highest performance in the whole range, demonstrating its high promise as an HTL. It can also be seen that when comparing organic HTLs, PEDOT:PSS shows higher efficiency than Spiro-OMeTAD at low temperatures (290–360 K). The general pattern of decrease in *PCE* with increasing temperature is consistent with earlier work [68,83,102]. Although the impact of defects is not considered directly in this study, we assume that the relatively weak perovskite crystal lattice may provoke the formation of defects; therefore, ionic defects in the lattice itself can be activated under the thermal impact. Accordingly, the accumulation of ionic defects may cause degradation of the crystalline structure of the perovskite film and the transport layers, which can significantly affect the solar cell stability [100].

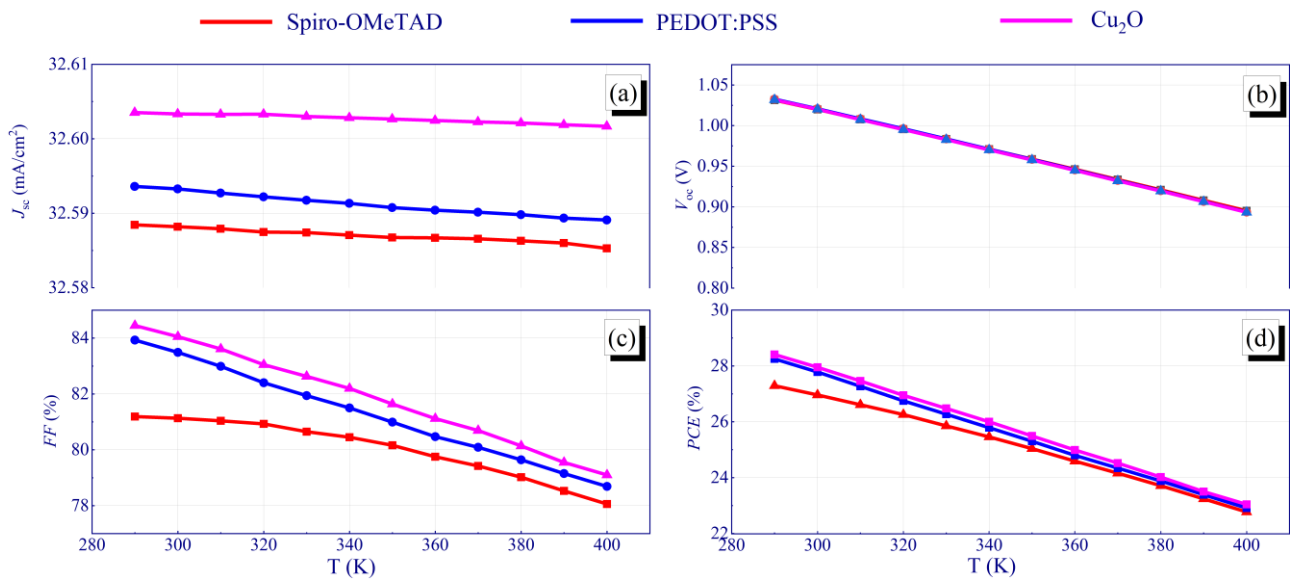


Figure 9. Influence of temperature on J_{sc} (a), V_{oc} (b), FF (c), PCE (d) for the perovskite solar cells with different hole-transport layers.

3.5. Comparison of J - V Characteristics for Different HTLs

To determine the optimal HTL among those studied, the J - V curves were simulated for various combinations of the TiO₂/CH₃NH₃SnI₃/HTL/Au structure (Figure 10).

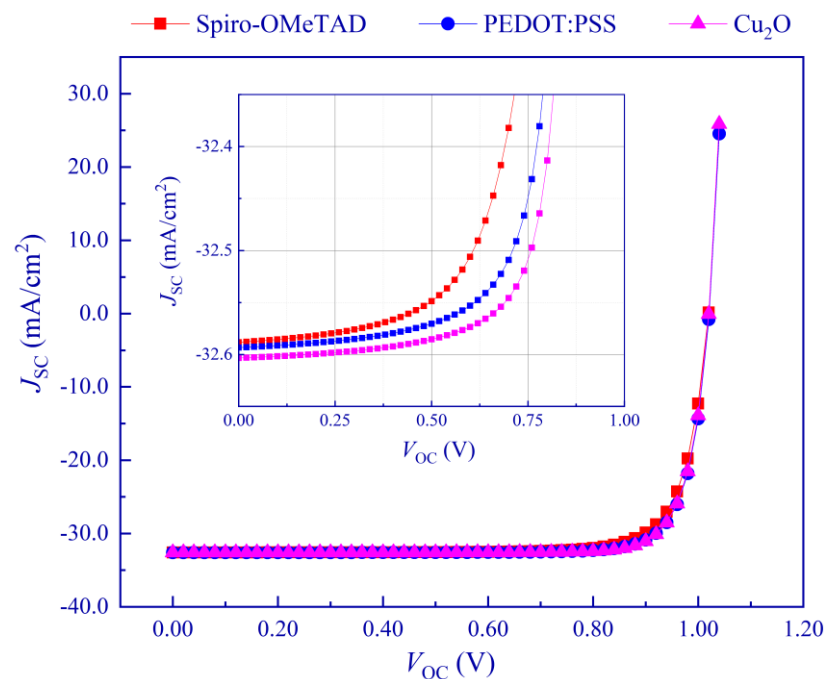


Figure 10. Current-voltage characteristics of perovskite solar cells with different hole-transport layers.

The Cu₂O based PSC shows the most optimal J - V characteristic curve. This is indicated by the lower series resistance and higher shunt resistance demonstrated by Structure 3. As a result, Cu₂O is shown to be a promising inorganic HTL for PSCs, whose relatively low cost and stability may also signal its high promise and economic feasibility in other applications.

3.6. Influence of the Thickness of the Light-Absorbing Layer on the Device Performance

Finally, an attempt was made to evaluate the impact of the absorbing layer thickness on the PSC performance. The perovskite thickness was varied in the range of 300–1300 nm. Figure 11 shows the PSC J - V characteristics for various thicknesses of the $\text{CH}_3\text{NH}_3\text{SnI}_3$ absorbing layer.

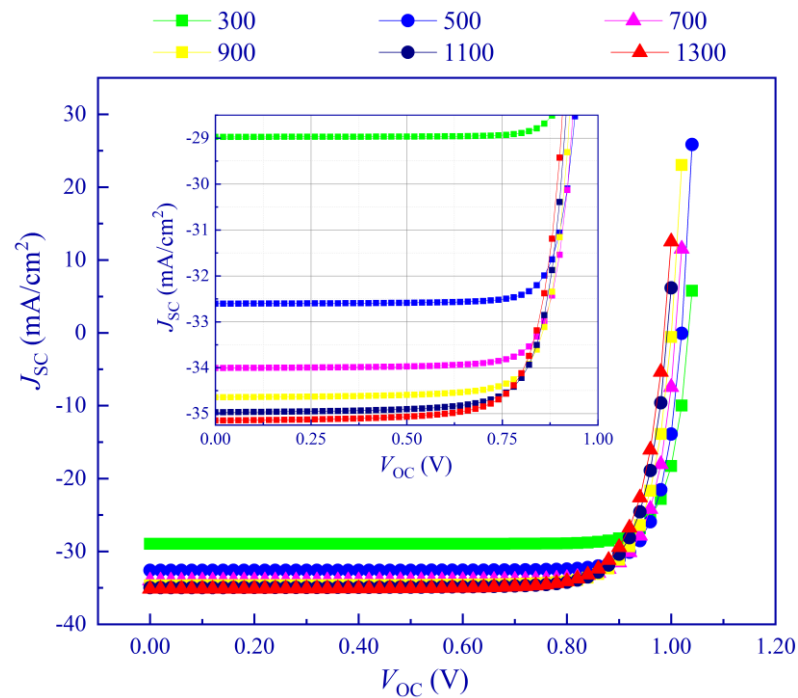


Figure 11. Current-voltage characteristic of a simulated photovoltaic cell $\text{FTO}/\text{TiO}_2/\text{CH}_3\text{NH}_3\text{SnI}_3/\text{Cu}_2\text{O}/\text{Au}$ with different thicknesses of the absorbing layer.

The simulation results are summarized in Figure 12, with the blue line indicating photovoltaic characteristics in the presence of interfacial defects (10^{10} cm^{-2}), and the red line—in their absence. According to Figure 12, interfacial defects do not result in any significant deterioration, but rather a small improvement. Figure 12a suggests that, as the thickness is increased in the range of 300–700 nm, a noticeable growth in J_{SC} is observed from $28.97 \text{ mA}/\text{cm}^2$ to $34.01 \text{ mA}/\text{cm}^2$ due to a higher optical absorption; upon the addition of interfacial defects this value rises by a further $0.10 \text{ mA}/\text{cm}^2$. Increasing the thickness from 700 nm to 1300 nm leads to a further small rise in J_{SC} by $1.14 \text{ mA}/\text{cm}^2$.

As shown in Figure 12b, V_{OC} decreases slightly as the thickness of the absorber layer increases throughout the studied range. It should be noted that the decrease in V_{OC} is directly related to the increase in J_{SC} , which directly affects carrier recombination. Figure 12c shows the variation in FF as a function of the absorber layer thickness. The monotonous decrease in FF for an increasingly thick absorber layer is explained by an increase in series resistance. Figure 12d shows the resulting PCE performance, affected by an increase in J_{SC} and reductions in V_{OC} and FF . In the range of 300–700 nm PCE shows a steady increase by more than 10%. However, at higher thicknesses up to 1300 nm, a moderate loss of PCE of about 2% is observed. Thus, 700 nm indicates the optimal device thickness under given conditions.

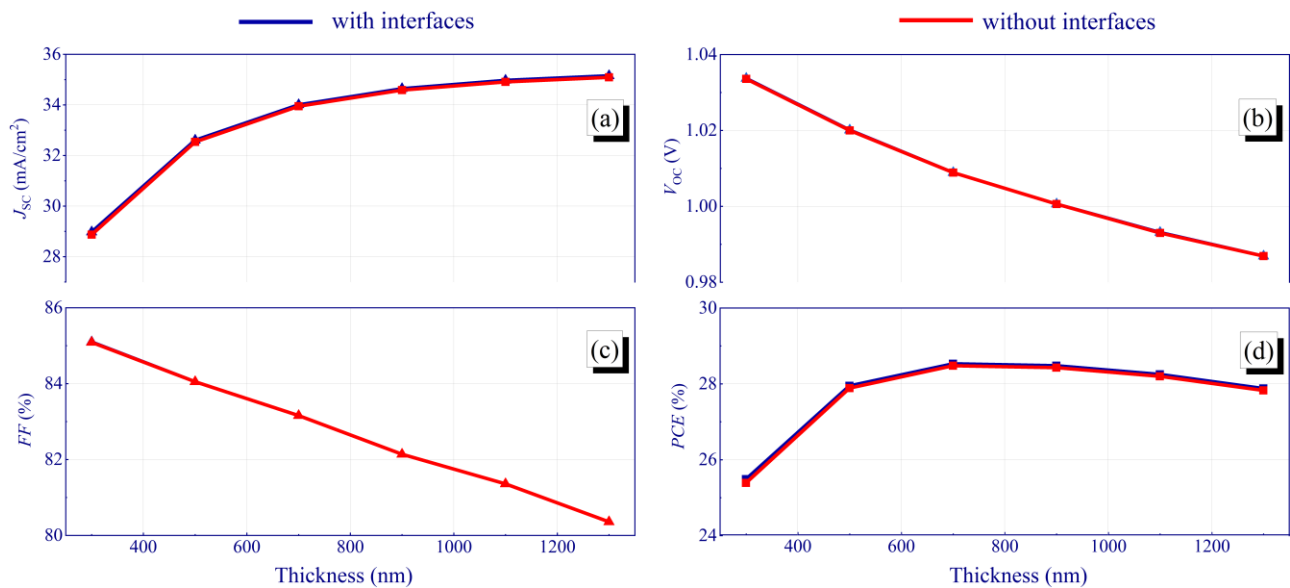


Figure 12. Influence of the perovskite absorbing layer thickness on J_{SC} (a), V_{OC} (b), FF (c), PCE (d).

4. Conclusions

The simulations focus on the influence of bulk defects within the absorbing layer, interfacial defects, temperature and thickness of the absorbing layer on the device performance. These factors were studied for three different HTLs, including Spiro-OMeTAD, PEDOT:PSS and Cu_2O , in order to determine the optimal transport layer, least sensitive towards performance deterioration. It has been found that the PSC works best at the room temperature of 300 K, in the absence of ionic contribution. For bulk defect densities larger than 10^{15} cm^{-3} , a decrease in the performance was observed for all the device structures. The tolerance limit for the density of interfacial defects at the $TiO_2/CH_3NH_3SnI_3$ (IL1) and $CH_3NH_3SnI_3/HTL$ (IL2) interfaces was 10^{14} cm^{-3} and 10^{10} cm^{-3} . Among the considered structures, the $TiO_2/CH_3NH_3SnI_3/Cu_2O$ structure shows the best defect resistance and the highest performance. The most suitable metallic contact was determined to be Pt, which provides high efficiency of 26.96%, 27.80% and 27.95% for structures with HTLs of Spiro-OMeTAD, PEDOT:PSS and Cu_2O , respectively. As a result of the study, the chosen optimal device structure was identified: $TiO_2/CH_3NH_3SnI_3/Cu_2O$ with $J_{SC} = 32.60 \text{ mA/cm}^2$, $V_{OC} = 1.02 \text{ V}$, $FF = 84.05\%$ and $PCE = 27.95\%$, which provide the high PCE and higher resistance towards both bulk and interfacial defects. This efficiency value is below the Shockley–Quisser limit of around 33% for the bandgap of the given perovskite absorber. It is, however, significantly higher than the current record experimental value of 14.6% for a tin perovskite solar cell [103]. Whilst the Shockley–Quisser limit assumes a number of simplifications, such as the absence of optical losses, non-radiative recombination and perfect carrier mobility, these factors can, to some extent, be accounted for in in-silico investigations. At the same time, the latter produce an “optimistic” performance limit for the given material properties with further improvements required regarding a realistic description of bulk, interface and surface recombination, the role of defects on carrier mobility and lifetime, as well as the impact of mobile ions on the device performance and stability. We therefore hope that the results of this work will help to reveal further approaches to achieve higher efficiency in tin-based perovskite solar cells.

Author Contributions: Conceptualization, Z.O., D.Y., A.A. and N.T.; methodology, Z.O., D.Y. and N.T.; software, Z.O.; formal analysis, Z.O., D.Y. and N.T.; investigation, Z.O., D.Y.; data curation, Z.O., D.Y. and N.T.; writing—original draft preparation, Z.O. and D.Y.; writing—review and editing, Z.O., D.Y., A.A. and N.T.; visualization, D.Y.; supervision, N.T.; project administration, A.A.

and N.T.; funding acquisition, A.A. All authors have read and agreed to the published version of the manuscript.

Funding: These studies have been carried out with the financial support of the Ministry of Education and Science of the Republic of Kazakhstan under grant AP08855738.

Institutional Review Board Statement: Not applicable.

Informed Consent Statement: Not applicable.

Data Availability Statement: Data will be made available upon a reasonable request to the corresponding author.

Acknowledgments: These studies have been carried out with the financial support of the Ministry of Education and Science of the Republic of Kazakhstan under grant AP08855738. The authors acknowledge the provision of SCAPS-1D software by Marc Burgelman. The authors acknowledge the graphic drawings to doctoral student Al Farabi Kazakh National University Golikov Oleg.

Conflicts of Interest: The authors declare no conflict of interest.

References

1. Green, M.A.; Hishikawa, Y.; Dunlop, E.D.; Levi, D.H.; Hohl-Ebinger, J.; Ho-Baillie, A.W.Y. Solar cell efficiency tables (version 52). *Prog. Photovolt. Res. Appl.* **2018**, *26*, 427–436. [\[CrossRef\]](#)
2. Yoshikawa, K.; Kawasaki, H.; Yoshida, W.; Irie, T.; Konishi, K.; Nakano, K.; Uto, T.; Adachi, D.; Kanematsu, M.; Uzu, H.; et al. Silicon heterojunction solar cell with interdigitated back contacts for a photoconversion efficiency over 26%. *Nat. Energy* **2017**, *2*, 17032. [\[CrossRef\]](#)
3. Elsmami, M.I.; Fatima, N.; Jallorina, M.P.A.; Sepeai, S.; Su'ait, M.S.; Ahmad Ludin, N.; Mat Teridi, M.A.; Sopian, K.; Ibrahim, M.A. Recent issues and configuration factors in perovskite-silicon tandem solar cells towards large scaling production. *Nanomaterials* **2021**, *11*, 3186. [\[CrossRef\]](#) [\[PubMed\]](#)
4. Alvarez, H.S.; Silva, A.R.; Espinola, L.C.J.; Vaz, A.R.; Diniz, J.A. NH₄ OH-B silicon texturing of periodic V-groove channels, upright, and inverted pyramids structures. *IEEE J. Photovolt.* **2021**, *11*, 570–574. [\[CrossRef\]](#)
5. Yuan, S.; Cui, Y.; Zhuang, Y.; Chen, P.; Hu, Y.; Yang, B.; Yu, Y.; Ren, Y.; Wang, W.; Chen, W.; et al. Passivated emitter and rear cell silicon solar cells with a front polysilicon passivating contacted selective emitter. *Phys. Status Solidi—Rapid Res. Lett.* **2021**, *15*, 2100057. [\[CrossRef\]](#)
6. Richter, A.; Müller, R.; Benick, J.; Feldmann, F.; Steinhauser, B.; Reichel, C.; Fell, A.; Bivour, M.; Hermle, M.; Glunz, S.W. Design rules for high-efficiency both-sides-contacted silicon solar cells with balanced charge carrier transport and recombination losses. *Nat. Energy* **2021**, *6*, 429–438. [\[CrossRef\]](#)
7. Owusu, P.A.; Asumadu-Sarkodie, S. A review of renewable energy sources, sustainability issues and climate change mitigation. *Cogent Eng.* **2016**, *3*, 1167990. [\[CrossRef\]](#)
8. Ramírez-Márquez, C.; Villicaña-García, E.; Cansino-Loeza, B.; Segovia-Hernández, J.G.; Ponce-Ortega, J.M. Inherent occupational health hazards in the production of solar grade silicon. *Process Saf. Environ. Prot.* **2020**, *142*, 285–294. [\[CrossRef\]](#)
9. Ramírez-Márquez, C.; Contreras-Zarazúa, G.; Martín, M.; Segovia-Hernández, J.G. Safety, economic, and environmental optimization applied to three processes for the production of solar-grade silicon. *ACS Sustain. Chem. Eng.* **2019**, *7*, 5355–5366. [\[CrossRef\]](#)
10. Momblona, C.; Gil-Escrig, L.; Bandiello, E.; Hutter, E.M.; Sessolo, M.; Lederer, K.; Blochwitz-Nimoth, J.; Bolink, H.J. Efficient vacuum deposited p-i-n and n-i-p perovskite solar cells employing doped charge transport layers. *Energy Environ. Sci.* **2016**, *9*, 3456–3463. [\[CrossRef\]](#)
11. Zhao, X.; Sun, Y.; Liu, S.; Chen, G.; Chen, P.; Wang, J.; Cao, W.; Wang, C. Humidity sensitivity behavior of CH₃NH₃PbI₃ perovskite. *Nanomaterials* **2022**, *12*, 523. [\[CrossRef\]](#) [\[PubMed\]](#)
12. Triolo, C.; De Giorgi, M.L.; Lorusso, A.; Creti, A.; Santangelo, S.; Lomascolo, M.; Anni, M.; Mazzeo, M.; Patané, S. Light emission properties of thermally evaporated CH₃NH₃PbBr₃ perovskite from nano- to macro-scale: Role of free and localized excitons. *Nanomaterials* **2022**, *12*, 211. [\[CrossRef\]](#) [\[PubMed\]](#)
13. Nayak, P.K.; Mahesh, S.; Snaith, H.J.; Cahen, D. Photovoltaic solar cell technologies: Analysing the state of the art. *Nat. Rev. Mater.* **2019**, *4*, 269–285. [\[CrossRef\]](#)
14. Zhou, D.; Zhou, T.; Tian, Y.; Zhu, X.; Tu, Y. Perovskite-based solar cells: Materials, methods, and future perspectives. *J. Nanomater.* **2018**, *2018*, 8148072. [\[CrossRef\]](#)
15. Hwang, T.; Lee, B.; Kim, J.; Lee, S.; Gil, B.; Yun, A.J.; Park, B. From nanostructural evolution to dynamic interplay of constituents: Perspectives for perovskite solar cells. *Adv. Mater.* **2018**, *30*, 1704208. [\[CrossRef\]](#) [\[PubMed\]](#)
16. Yoo, J.J.; Seo, G.; Chua, M.R.; Park, T.G.; Lu, Y.; Rotermund, F.; Kim, Y.-K.; Moon, C.S.; Jeon, N.J.; Correa-Baena, J.-P.; et al. Efficient perovskite solar cells via improved carrier management. *Nature* **2021**, *590*, 587–593. [\[CrossRef\]](#)
17. Li, N.; Niu, X.; Li, L.; Wang, H.; Huang, Z.; Zhang, Y.; Chen, Y.; Zhang, X.; Zhu, C.; Zai, H.; et al. Liquid medium annealing for fabricating durable perovskite solar cells with improved reproducibility. *Science* **2021**, *373*, 561–567. [\[CrossRef\]](#)

18. Lee, K.-M.; Chan, S.-H.; Chiu, W.-H.; Ahn, S.; Ting, C.-C.; Chang, Y.-H.; Suryanarayanan, V.; Wu, M.-C.; Liu, C.-Y. Reducing defects in organic-lead halide perovskite film by delayed thermal annealing combined with KI/I₂ for efficient perovskite solar cells. *Nanomaterials* **2021**, *11*, 1607. [[CrossRef](#)]
19. Park, H.H. Efficient and stable perovskite solar cells based on inorganic hole transport materials. *Nanomaterials* **2021**, *12*, 112. [[CrossRef](#)]
20. Wu, J.; Li, Y.; Li, Y.; Xie, W.; Shi, J.; Li, D.; Cheng, S.; Meng, Q. Using hysteresis to predict the charge recombination properties of perovskite solar cells. *J. Mater. Chem. A* **2021**, *9*, 6382–6392. [[CrossRef](#)]
21. Yang, D.; Zhang, G.; Lai, R.; Cheng, Y.; Lian, Y.; Rao, M.; Huo, D.; Lan, D.; Zhao, B.; Di, D. Germanium-lead perovskite light-emitting diodes. *Nat. Commun.* **2021**, *12*, 4295. [[CrossRef](#)] [[PubMed](#)]
22. Dos Santos Rosa, E.H.; Kowalski, E.L.; Ribeiro Barrozo Toledo, L.F. Simulation of organic solar cells's power conversion efficiency. *Sol. Energy* **2021**, *221*, 483–487. [[CrossRef](#)]
23. Wei, H.; Qiu, P.; Li, Y.; He, Y.; Peng, M.; Zheng, X.; Liu, X. Challenges and strategies of all-inorganic lead-free halide perovskite solar cells. *Ceram. Int.* **2022**, *48*, 5876–5891. [[CrossRef](#)]
24. Li, J.; Cao, H.-L.; Jiao, W.-B.; Wang, Q.; Wei, M.; Cantone, I.; Lü, J.; Abate, A. Biological impact of lead from halide perovskites reveals the risk of introducing a safe threshold. *Nat. Commun.* **2020**, *11*, 310. [[CrossRef](#)] [[PubMed](#)]
25. Montoya De Los Santos, I.; Cortina-Marrero, H.J.; Ruíz-Sánchez, M.A.; Hechavarría-Difur, L.; Sánchez-Rodríguez, F.J.; Courel, M.; Hu, H. Optimization of CH₃NH₃PbI₃ perovskite solar cells: A theoretical and experimental study. *Sol. Energy* **2020**, *199*, 198–205. [[CrossRef](#)]
26. Cao, W.; Hu, Z.; Lin, Z.; Guo, X.; Su, J.; Chang, J.; Hao, Y. Defects and doping engineering towards high performance lead-free or lead-less perovskite solar cells. *J. Energy Chem.* **2022**, *68*, 420–438. [[CrossRef](#)]
27. Chandra, P.; Mandal, S.K. Morphology controlled (CH₃NH₃)₃Bi₂Cl₉ thin film for lead free perovskite solar cell. *Phys. B Condens. Matter* **2022**, *625*, 413536. [[CrossRef](#)]
28. Bai, F.; Hu, Y.; Hu, Y.; Qiu, T.; Miao, X.; Zhang, S. Lead-free, air-stable ultrathin Cs₃Bi₂I₉ perovskite nanosheets for solar cells. *Sol. Energy Mater. Sol. Cells* **2018**, *184*, 15–21. [[CrossRef](#)]
29. Turkevych, I.; Kazaoui, S.; Ito, E.; Urano, T.; Yamada, K.; Tomiyasu, H.; Yamagishi, H.; Kondo, M.; Aramaki, S. Photovoltaic ruddorffites: Lead-free silver bismuth halides alternative to hybrid lead halide perovskites. *ChemSusChem* **2017**, *10*, 3754–3759. [[CrossRef](#)]
30. Krishnamoorthy, T.; Ding, H.; Yan, C.; Leong, W.L.; Baikie, T.; Zhang, Z.; Sherburne, M.; Li, S.; Asta, M.; Mathews, N.; et al. Lead-free germanium iodide perovskite materials for photovoltaic applications. *J. Mater. Chem. A* **2015**, *3*, 23829–23832. [[CrossRef](#)]
31. Ünlü, F.; Deo, M.; Mathur, S.; Kirchartz, T.; Kulkarni, A. Bismuth-based halide perovskite and perovskite-inspired light absorbing materials for photovoltaics. *J. Phys. D. Appl. Phys.* **2022**, *55*, 113002. [[CrossRef](#)]
32. Toshniwal, A.; Kheraj, V. Development of organic-inorganic tin halide perovskites: A review. *Sol. Energy* **2017**, *149*, 54–59. [[CrossRef](#)]
33. Giustino, F.; Snaith, H.J. Toward lead-free perovskite solar cells. *ACS Energy Lett.* **2016**, *1*, 1233–1240. [[CrossRef](#)]
34. Abu Baker, A.M.; Boltaev, G.S.; Iqbal, M.; Pylnev, M.; Hamdan, N.M.; Alnaser, A.S. Giant third-order nonlinear response of mixed perovskite nanocrystals. *Materials* **2022**, *15*, 389. [[CrossRef](#)]
35. Pitaro, M.; Tekelenburg, E.K.; Shao, S.; Loi, M.A. Tin halide perovskites: From fundamental properties to solar cells. *Adv. Mater.* **2022**, *34*, 2105844. [[CrossRef](#)]
36. Singh, S.; Kabra, D. Comparative study of recombination dynamics in optimized composition of Sn- versus Pb-based perovskite solar cells. *ACS Appl. Mater. Interfaces* **2021**, *13*, 42297–42306. [[CrossRef](#)]
37. Roknuzzaman, M.; Ostrikov, K.; Wang, H.; Du, A.; Tesfamichael, T. Towards lead-free perovskite photovoltaics and optoelectronics by ab-initio simulations. *Sci. Rep.* **2017**, *7*, 14025. [[CrossRef](#)]
38. Le Corre, V.M.; Stolterfoht, M.; Perdigón Toro, L.; Feuerstein, M.; Wolff, C.; Gil-Escrig, L.; Bolink, H.J.; Neher, D.; Koster, L.J.A. Charge transport layers limiting the efficiency of perovskite solar cells: How to optimize conductivity, doping, and thickness. *ACS Appl. Energy Mater.* **2019**, *2*, 6280–6287. [[CrossRef](#)]
39. Braun, S.; Salaneck, W.R.; Fahlman, M. Energy-level alignment at organic/metal and organic/organic interfaces. *Adv. Mater.* **2009**, *21*, 1450–1472. [[CrossRef](#)]
40. Deepthi Jayan, K. Design and comparative performance analysis of high-efficiency lead-based and lead-free perovskite solar cells. *Phys. Status Solidi* **2022**, *219*, 2100606. [[CrossRef](#)]
41. Deepthi Jayan, K.; Sebastian, V. Modelling and comparative performance analysis of tin based mixed halide perovskite solar cells with IGZO and CuO as charge transport layers. *Int. J. Energy Res.* **2021**, *45*, 16618–16632. [[CrossRef](#)]
42. Chen, Q.; Ni, Y.; Dou, X.; Yoshinori, Y. The effect of energy level of transport layer on the performance of ambient air prepared perovskite solar cell: A SCAPS-1D simulation study. *Crystals* **2022**, *12*, 68. [[CrossRef](#)]
43. Rombach, F.M.; Haque, S.A.; Macdonald, T.J. Lessons learned from spiro-OMeTAD and PTAA in perovskite solar cells. *Energy Environ. Sci.* **2021**, *14*, 5161–5190. [[CrossRef](#)]
44. Mahapatra, B.; Krishna, R.V.; Laxmi, Patel, P.K. Design and optimization of CuSCN/CH₃NH₃PbI₃/TiO₂ perovskite solar cell for efficient performance. *Opt. Commun.* **2022**, *504*, 127496. [[CrossRef](#)]

45. Farooq, W.; Alshahrani, T.; Kazmi, S.A.A.; Iqbal, J.; Khan, H.A.; Khan, M.; Raja, A.A.; ur Rehman, A. Materials optimization for thin-film copper indium gallium selenide (CIGS) solar cell based on distributed bragg reflector. *Optik* **2021**, *227*, 165987. [[CrossRef](#)]
46. Yang, H.-Y.; Rho, W.-Y.; Lee, S.; Kim, S.; Hahn, Y.-B. TiO₂ nanoparticles/nanotubes for efficient light harvesting in perovskite solar cells. *Nanomaterials* **2019**, *9*, 326. [[CrossRef](#)]
47. Kung, P.; Li, M.; Lin, P.; Chiang, Y.; Chan, C.; Guo, T.; Chen, P. A review of inorganic hole transport materials for perovskite solar cells. *Adv. Mater. Interfaces* **2018**, *5*, 1800882. [[CrossRef](#)]
48. Gil, B.; Yun, A.J.; Lee, Y.; Kim, J.; Lee, B.; Park, B. Recent progress in inorganic hole transport materials for efficient and stable perovskite solar cells. *Electron. Mater. Lett.* **2019**, *15*, 505–524. [[CrossRef](#)]
49. Arumugam, G.M.; Karunakaran, S.K.; Liu, C.; Zhang, C.; Guo, F.; Wu, S.; Mai, Y. Inorganic hole transport layers in inverted perovskite solar cells: A review. *Nano Sel.* **2021**, *2*, 1081–1116. [[CrossRef](#)]
50. Xu, B.; Zhu, H.; Bao, H.; Cao, X.; Dong, Y.; Zhang, Y.; Yin, G.; Li, X.; Wang, S. Bifunctional spiro-fluorene/heterocycle cored hole-transporting materials: Role of the heteroatom on the photovoltaic performance of perovskite solar cells. *Chem. Eng. J.* **2022**, *431*, 133371. [[CrossRef](#)]
51. Roy, P.; Raoui, Y.; Khare, A. Design and simulation of efficient tin based perovskite solar cells through optimization of selective layers: Theoretical insights. *Opt. Mater.* **2022**, *125*, 112057. [[CrossRef](#)]
52. Singh, N.; Agarwal, A.; Agarwal, M. Performance evaluation of lead-free double-perovskite solar cell. *Opt. Mater.* **2021**, *114*, 110964. [[CrossRef](#)]
53. Kanoun, A.-A.; Kanoun, M.B.; Merad, A.E.; Goumri-Said, S. Toward development of high-performance perovskite solar cells based on CH₃NH₃GeI₃ using computational approach. *Sol. Energy* **2019**, *182*, 237–244. [[CrossRef](#)]
54. Song, W.; Rakocevic, L.; Thiruvallur Eachambadi, R.; Qiu, W.; Bastos, J.P.; Gehlhaar, R.; Kuang, Y.; Hadipour, A.; Aernouts, T.; Poortmans, J. Improving the morphology stability of spiro-OMeTAD films for enhanced thermal stability of perovskite solar cells. *ACS Appl. Mater. Interfaces* **2021**, *13*, 44294–44301. [[CrossRef](#)] [[PubMed](#)]
55. Ibanez, J.G.; Rincón, M.E.; Gutierrez-Granados, S.; Chahma, M.; Jaramillo-Quintero, O.A.; Frontana-Uribe, B.A. Conducting polymers in the fields of energy, environmental remediation, and chemical–chiral sensors. *Chem. Rev.* **2018**, *118*, 4731–4816. [[CrossRef](#)] [[PubMed](#)]
56. Anrango-Camacho, C.; Pavón-Ipiales, K.; Frontana-Uribe, B.A.; Palma-Cando, A. Recent advances in hole-transporting layers for organic solar cells. *Nanomaterials* **2022**, *12*, 443. [[CrossRef](#)]
57. Wang, J.; Yu, H.; Hou, C.; Zhang, J. Solution-Processable PEDOT:PSS:α-In₂Se₃ with enhanced conductivity as a hole transport layer for high-performance polymer solar cells. *ACS Appl. Mater. Interfaces* **2020**, *12*, 26543–26554. [[CrossRef](#)]
58. Lee, S.W.; Lee, Y.S.; Heo, J.; Siah, S.C.; Chua, D.; Brandt, R.E.; Kim, S.B.; Mailoa, J.P.; Buonassisi, T.; Gordon, R.G. Improved Cu₂O-based solar cells using atomic layer deposition to control the Cu oxidation state at the p-n junction. *Adv. Energy Mater.* **2014**, *4*, 1301916. [[CrossRef](#)]
59. Murali, D.S.; Kumar, S.; Choudhary, R.J.; Wadikar, A.D.; Jain, M.K.; Subrahmanyam, A. Synthesis of Cu₂O from CuO thin films: Optical and electrical properties. *AIP Adv.* **2015**, *5*, 047143. [[CrossRef](#)]
60. Scanlon, D.O.; Morgan, B.J.; Watson, G.W.; Walsh, A. Acceptor levels in *p*-Type Cu₂O: Rationalizing theory and experiment. *Phys. Rev. Lett.* **2009**, *103*, 096405. [[CrossRef](#)]
61. Zuo, C.; Ding, L. Solution-processed Cu₂O and CuO as hole transport materials for efficient perovskite solar cells. *Small* **2015**, *11*, 5528–5532. [[CrossRef](#)] [[PubMed](#)]
62. He, Y.; Xu, L.; Yang, C.; Guo, X.; Li, S. Design and numerical investigation of a lead-free inorganic layered double perovskite Cs₄CuSb₂Cl₁₂ nanocrystal solar cell by SCAPS-1D. *Nanomaterials* **2021**, *11*, 2321. [[CrossRef](#)] [[PubMed](#)]
63. Samiul Islam, M.; Sobayel, K.; Al-Kahtani, A.; Islam, M.A.; Muhammad, G.; Amin, N.; Shahiduzzaman, M.; Akhtaruzzaman, M. Defect study and modelling of SnX₃-based perovskite solar cells with SCAPS-1D. *Nanomaterials* **2021**, *11*, 1218. [[CrossRef](#)] [[PubMed](#)]
64. Yao, H.; Liu, L. Design and optimize the performance of self-powered photodetector based on PbS/TiS₃ heterostructure by SCAPS-1D. *Nanomaterials* **2022**, *12*, 325. [[CrossRef](#)]
65. Moiz, S.A. Optimization of hole and electron transport layer for highly efficient lead-free Cs₂TiBr₆-based perovskite solar cell. *Photonics* **2021**, *9*, 23. [[CrossRef](#)]
66. Piñón Reyes, A.C.; Ambrosio Lázaro, R.C.; Monfil Leyva, K.; Luna López, J.A.; Flores Méndez, J.; Heredia Jiménez, A.H.; Muñoz Zurita, A.L.; Severiano Carrillo, F.; Ojeda Durán, E. Study of a lead-free perovskite solar cell using CZTS as HTL to achieve a 20% PCE by SCAPS-1D simulation. *Micromachines* **2021**, *12*, 1508. [[CrossRef](#)]
67. Zyoud, S.H.; Zyoud, A.H.; Ahmed, N.M.; Prasad, A.R.; Khan, S.N.; Abdelkader, A.F.I.; Shahwan, M. Numerical modeling of high conversion efficiency FTO/ZnO/CdS/CZTS/MO thin film-based solar cells: Using SCAPS-1D software. *Crystals* **2021**, *11*, 1468. [[CrossRef](#)]
68. Mottakin, M.; Sobayel, K.; Sarkar, D.; Alkhamash, H.; Alharthi, S.; Techato, K.; Shahiduzzaman, M.; Amin, N.; Sopian, K.; Akhtaruzzaman, M. Design and modelling of eco-friendly CH₃NH₃SnI₃-based perovskite solar cells with suitable transport layers. *Energies* **2021**, *14*, 7200. [[CrossRef](#)]
69. Raoui, Y.; Ez-Zahraouy, H.; Tahiri, N.; El Bounagui, O.; Ahmad, S.; Kazim, S. Performance analysis of MAPbI₃ based perovskite solar cells employing diverse charge selective contacts: Simulation study. *Sol. Energy* **2019**, *193*, 948–955. [[CrossRef](#)]

70. Lin, L.; Jiang, L.; Li, P.; Xiong, H.; Kang, Z.; Fan, B.; Qiu, Y. Simulated development and optimized performance of CsPbI₃ based all-inorganic perovskite solar cells. *Sol. Energy* **2020**, *198*, 454–460. [[CrossRef](#)]
71. Patel, P.K. Device simulation of highly efficient eco-friendly CH₃NH₃SnI₃ perovskite solar cell. *Sci. Rep.* **2021**, *11*, 3082. [[CrossRef](#)] [[PubMed](#)]
72. Rono, N.; Merad, A.E.; Kibet, J.K.; Martincigh, B.S.; Nyamori, V.O. A theoretical investigation of the effect of the hole and electron transport materials on the performance of a lead-free perovskite solar cell based on CH₃NH₃SnI₃. *J. Comput. Electron.* **2021**, *20*, 993–1005. [[CrossRef](#)]
73. Chen, M.; Ju, M.-G.; Garces, H.F.; Carl, A.D.; Ono, L.K.; Hawash, Z.; Zhang, Y.; Shen, T.; Qi, Y.; Grimm, R.L.; et al. Highly stable and efficient all-inorganic lead-free perovskite solar cells with native-oxide passivation. *Nat. Commun.* **2019**, *10*, 16. [[CrossRef](#)] [[PubMed](#)]
74. Abd Mutalib, M.; Ahmad Ludin, N.; Nik Ruzalman, N.A.A.; Barrioz, V.; Sepeai, S.; Mat Teridi, M.A.; Su'ait, M.S.; Ibrahim, M.A.; Sopian, K. Progress towards highly stable and lead-free perovskite solar cells. *Mater. Renew. Sustain. Energy* **2018**, *7*, 7. [[CrossRef](#)]
75. Tailor, N.K.; Kar, S.; Mishra, P.; These, A.; Kupfer, C.; Hu, H.; Awais, M.; Saidaminov, M.; Dar, M.I.; Brabec, C.; et al. Advances in lead-free perovskite single crystals: Fundamentals and applications. *ACS Mater. Lett.* **2021**, *3*, 1025–1080. [[CrossRef](#)]
76. ABENA, A.M.N.; NGOUPO, A.T.; ABEGA, F.X.A.; NDJAKA, J.M.B. Numerical investigation of solar cells based on hybrid organic cation perovskite with inorganic HTL via SCAPS-1D. *Chinese J. Phys.* **2022**, *76*, 94–109. [[CrossRef](#)]
77. Al-Hattab, M.; Moudou, L.; Khenfouch, M.; Bajjou, O.; Chrafi, Y.; Rahmani, K. Numerical simulation of a new heterostructure CIGS/GaSe solar cell system using SCAPS-1D software. *Sol. Energy* **2021**, *227*, 13–22. [[CrossRef](#)]
78. Houimi, A.; Gezgin, S.Y.; Mercimek, B.; Kiliç, H.Ş. Numerical analysis of CZTS/n-Si solar cells using SCAPS-1D. A comparative study between experimental and calculated outputs. *Opt. Mater.* **2021**, *121*, 111544. [[CrossRef](#)]
79. Moiz, S.A.; Alahmadi, A.N.M. Design of dopant and lead-free novel perovskite solar cell for 16.85% efficiency. *Polymers* **2021**, *13*, 2110. [[CrossRef](#)]
80. Burgelman, M.; Decock, K.; Khelifi, S.; Abass, A. Advanced electrical simulation of thin film solar cells. *Thin Solid Films* **2013**, *535*, 296–301. [[CrossRef](#)]
81. Verschraegen, J.; Burgelman, M. Numerical modeling of intra-band tunneling for heterojunction solar cells in scaps. *Thin Solid Films* **2007**, *515*, 6276–6279. [[CrossRef](#)]
82. Hao, L.; Zhou, M.; Song, Y.; Ma, X.; Wu, J.; Zhu, Q.; Fu, Z.; Liu, Y.; Hou, G.; Li, T. Tin-based perovskite solar cells: Further improve the performance of the electron transport layer-free structure by device simulation. *Sol. Energy* **2021**, *230*, 345–354. [[CrossRef](#)]
83. Deepthi Jayan, K.; Sebastian, V. Comprehensive device modelling and performance analysis of MASnI₃ based perovskite solar cells with diverse ETM, HTM and back metal contacts. *Sol. Energy* **2021**, *217*, 40–48. [[CrossRef](#)]
84. Ito, N.; Kamarudin, M.A.; Hirotani, D.; Zhang, Y.; Shen, Q.; Ogomi, Y.; Iikubo, S.; Minemoto, T.; Yoshino, K.; Hayase, S. Mixed Sn–Ge perovskite for enhanced perovskite solar cell performance in air. *J. Phys. Chem. Lett.* **2018**, *9*, 1682–1688. [[CrossRef](#)]
85. Minemoto, T.; Kawano, Y.; Nishimura, T.; Shen, Q.; Yoshino, K.; Iikubo, S.; Hayase, S.; Chantana, J. Theoretical analysis of band alignment at back junction in Sn–Ge perovskite solar cells with inverted p-i-n structure. *Sol. Energy Mater. Sol. Cells* **2020**, *206*, 110268. [[CrossRef](#)]
86. Noel, N.K.; Abate, A.; Stranks, S.D.; Parrott, E.S.; Burlakov, V.M.; Goriely, A.; Snaith, H.J. Enhanced photoluminescence and solar cell performance via lewis base passivation of organic–inorganic lead halide perovskites. *ACS Nano* **2014**, *8*, 9815–9821. [[CrossRef](#)]
87. Kearney, K.; Seo, G.; Matsushima, T.; Adachi, C.; Ertekin, E.; Rockett, A. Computational analysis of the interplay between deep level traps and perovskite solar cell efficiency. *J. Am. Chem. Soc.* **2018**, *140*, 15655–15660. [[CrossRef](#)]
88. Joshi, P.H.; Zhang, L.; Hossain, I.M.; Abbas, H.A.; Kottokaran, R.; Nehra, S.P.; Dhaka, M.; Noack, M.; Dalal, V.L. The physics of photon induced degradation of perovskite solar cells. *AIP Adv.* **2016**, *6*, 115114. [[CrossRef](#)]
89. Adinolfi, V.; Yuan, M.; Comin, R.; Thibau, E.S.; Shi, D.; Saidaminov, M.I.; Kanjanaboos, P.; Kopilovic, D.; Hoogland, S.; Lu, Z.-H.; et al. The in-gap electronic state spectrum of methylammonium lead iodide single-crystal perovskites. *Adv. Mater.* **2016**, *28*, 3406–3410. [[CrossRef](#)]
90. De Quilettes, D.W.; Vorpahl, S.M.; Stranks, S.D.; Nagaoka, H.; Eperon, G.E.; Ziffer, M.E.; Snaith, H.J.; Ginger, D.S. Impact of microstructure on local carrier lifetime in perovskite solar cells. *Science* **2015**, *348*, 683–686. [[CrossRef](#)]
91. Chowdhury, M.S.; Shahahmadi, S.A.; Chelvanathan, P.; Tiong, S.K.; Amin, N.; Techato, K.; Nuthammachot, N.; Chowdhury, T.; Suklueng, M. Effect of deep-level defect density of the absorber layer and n/i interface in perovskite solar cells by SCAPS-1D. *Results Phys.* **2020**, *16*, 102839. [[CrossRef](#)]
92. Walukiewicz, W.; Rey-Stolle, I.; Han, G.; Jaquez, M.; Broberg, D.; Xie, W.; Sherburne, M.; Mathews, N.; Asta, M. Bistable amphoteric native defect model of perovskite photovoltaics. *J. Phys. Chem. Lett.* **2018**, *9*, 3878–3885. [[CrossRef](#)] [[PubMed](#)]
93. Jiang, Q.; Zhao, Y.; Zhang, X.; Yang, X.; Chen, Y.; Chu, Z.; Ye, Q.; Li, X.; Yin, Z.; You, J. Surface passivation of perovskite film for efficient solar cells. *Nat. Photonics* **2019**, *13*, 460–466. [[CrossRef](#)]
94. Yoo, J.J.; Wieghold, S.; Sponseller, M.C.; Chua, M.R.; Bertram, S.N.; Hartono, N.T.P.; Tresback, J.S.; Hansen, E.C.; Correa-Baena, J.-P.; Bulović, V.; et al. An interface stabilized perovskite solar cell with high stabilized efficiency and low voltage loss. *Energy Environ. Sci.* **2019**, *12*, 2192–2199. [[CrossRef](#)]
95. Zheng, X.; Chen, B.; Dai, J.; Fang, Y.; Bai, Y.; Lin, Y.; Wei, H.; Zeng, X.C.; Huang, J. Defect passivation in hybrid perovskite solar cells using quaternary ammonium halide anions and cations. *Nat. Energy* **2017**, *2*, 17102. [[CrossRef](#)]

96. Wolff, C.M.; Caprioglio, P.; Stolterfoht, M.; Neher, D. Nonradiative recombination in perovskite solar cells: The role of interfaces. *Adv. Mater.* **2019**, *31*, 1902762. [[CrossRef](#)]
97. Samantaray, M.R.; Rana, N.K.; Kumar, A.; Ghosh, D.S.; Chander, N. Stability study of large-area perovskite solar cells fabricated with copper as low-cost metal contact. *Int. J. Energy Res.* **2022**, *46*, 1250–1262. [[CrossRef](#)]
98. Çaldıran, Z. Modification of Schottky barrier height using an inorganic compound interface layer for various contact metals in the metal/p-Si device structure. *J. Alloys Compd.* **2021**, *865*, 158856. [[CrossRef](#)]
99. Lin, C.-H.; Li, T.-Y.; Cheng, B.; Liu, C.; Yang, C.-W.; Ke, J.-J.; Wei, T.-C.; Li, L.-J.; Fratolocchi, A.; He, J.-H. Metal contact and carrier transport in single crystalline CH₃NH₃PbBr₃ perovskite. *Nano Energy* **2018**, *53*, 817–827. [[CrossRef](#)]
100. Zai, H.; Ma, Y.; Chen, Q.; Zhou, H. Ion migration in halide perovskite solar cells: Mechanism, characterization, impact and suppression. *J. Energy Chem.* **2021**, *63*, 528–549. [[CrossRef](#)]
101. Cheng, Y.; Liu, X.; Guan, Z.; Li, M.; Zeng, Z.; Li, H.; Tsang, S.; Aberle, A.G.; Lin, F. Revealing the degradation and self-healing mechanisms in perovskite solar cells by sub-bandgap external quantum efficiency spectroscopy. *Adv. Mater.* **2021**, *33*, 2006170. [[CrossRef](#)] [[PubMed](#)]
102. Roy, P.; Tiwari, S.; Khare, A. An investigation on the influence of temperature variation on the performance of tin (Sn) based perovskite solar cells using various transport layers and absorber layers. *Results Opt.* **2021**, *4*, 100083. [[CrossRef](#)]
103. Jiang, X.; Li, H.; Zhou, Q.; Wei, Q.; Wei, M.; Jiang, L.; Wang, Z.; Peng, Z.; Wang, F.; Zang, Z.; et al. One-step synthesis of SnI₂·(DMSO)_x adducts for high-performance tin perovskite solar cells. *J. Am. Chem. Soc.* **2021**, *143*, 10970–10976. [[CrossRef](#)] [[PubMed](#)]